Gyrokinetic simulation of collisionless trapped-electron mode turbulence

Tilman Dannert[a] and Frank Jenko
Max-Planck Institut für Plasmaphysik, EURATOM Association, 85748 Garching, Germany

(Received 8 April 2005; accepted 12 May 2005; published online 7 July 2005)

Some basic properties of collisionless, trapped-electron mode turbulence in tokamaks are investigated by means of massively parallel gyrokinetic Vlasov simulations. In particular, the spatial structure and wave number spectra of various fluctuating plasma quantities are presented and discussed. An analysis of several cross phase relations supports the view that the transport-dominating scales may be interpreted in terms of remnants of linear modes. In a few test cases, zonal flows are artificially suppressed, demonstrating that their influence on the transport level is small. Finally, the dependence of the latter on several plasma parameters is studied. © *2005 American Institute of Physics*. [DOI: 10.1063/1.1947447]

I. INTRODUCTION

It is generally believed that turbulence driven by trapped-electron modes (TEMs) is largely responsible for the experimentally observed electron heat (and particle) transport in magnetized fusion plasmas.[1] TEMs involve electrons which are magnetically trapped in the low-field (outboard) region of a tokamak. They are driven by electron pressure gradients in the presence of magnetic curvature.[2] Despite their importance, to date not much is known about their nonlinear behavior. Here, we present a systematic study of TEM turbulence, employing massively parallel gyrokinetic Vlasov simulations and retaining both trapped and passing electrons.

In the last 10–15 years, core turbulence studies have focused mainly on ion temperature gradient (ITG) modes with adiabatic (i.e., Boltzmann) electrons.[3,4] This simplification has two main advantages. First, the resulting dynamics are somewhat less complex and therefore more accessible to analysis, and second, the resulting equations are easier to solve numerically, mainly because of the lack of fast parallel electron motion. The drawback of this approach is that both the particle and the electron heat flux vanish identically in the adiabatic limit.

Having unravelled many interesting and surprising features of adiabatic ITG turbulence, the next step was/is to add nonadiabatic electrons. That this is more than a small correction as was shown, e.g., by Sydora *et al.*[5] They performed global gyrokinetic simulations of ITG turbulence, considering the passing electrons to be adiabatic but including trapped electrons. In the framework of this model, they found an increase of the ion heat transport by a factor of 2–3 with respect to the fully adiabatic reference case. Similar results were obtained by Beer and Hammett[6] who introduced bounce-averaged trapped electrons into their gyrofluid computations. More recently, the first gyrokinetic simulations retaining both trapped and passing electrons have been performed.[7–9]

Besides modifying ITG modes, nonadiabatic electrons have yet another important effect, namely, they introduce TEMs. Depending on the local plasma parameters, ITG modes and TEMs may either coexist or else be the only linear microinstabilty at ion Larmor radius scales. In this context, the key parameters are the (normalized) gradients of the background density, R/L_n, and electron and ion temperature, R/L_{T_e} and R/L_{T_i}. TEMs are driven by R/L_{T_e} and/or R/L_n, whereas ITG modes are driven by R/L_{T_i} and suppressed by R/L_n. As is well known, there exist nonuniversal instability thresholds in all of these quantities. In order to investigate pure TEM turbulence, one may set R/L_{T_i} to zero. This limiting case will be the focus in the present paper. It should be noted that such a situation is by no means artificial. Actually, in the last few years a lot of experiments have been carried out with dominant central electron heating.[10–13] In these discharges, the ions are rather cold, and ITG modes are linearly stable while TEMs are not. The more general case of TEMs coexisting with ITG modes is left for future studies.

The present paper is organized as follows. In Sec. II, the basic gyrokinetic equations are presented along with a brief description of the GENE code—on which this work is based—and a list of numerical and physical parameters. In Sec. III, we present and discuss various nonlinear simulation results, emphasizing some fundamental characteristics of collisionless TEM turbulence. Then, in Sec. IV, some parameter dependencies are studied. Section V contains a brief summary of key results along with some conclusions.

II. THE GYROKINETIC MODEL

A. Basic equations

The simulations presented below are based on the gyrokinetic Vlasov code GENE. It solves the nonlinear gyrokinetic equations[14–16] on a fixed grid in five-dimensional phase space (plus time). The independent variables are normalized according to Table I, with the ion sound scale $\rho_s=c_s/\Omega_i$, the ion Larmor frequency $\Omega_i=eB/m_ic$, the ion sound speed $c_s=\sqrt{T_{e0}/m_i}$, the thermal velocity $v_{T_j}=\sqrt{2T_{j0}/m_j}$ of species j $(j=e,i)$, the safety factor q, the major radius R, and a typical perpendicular equilibrium scale length $L_\perp$. The equilibrium magnetic field is taken to be $B=\hat{B}B_{\mathrm{ref}}$, where B_{ref} is the magnetic field on the magnetic axis and $\hat{B}$ describes the variation

[a]Electronic mail: Tilman.Dannert@ipp.mpg.de

TABLE I. Normalization of the independent variables.

t	x,y	z	$v_\parallel$	μ
$L_\perp/c_s$	ρ_s	qR	v_{Tj}	T_{j0}/B_{ref}

TABLE II. Normalization of the dependent variables.

F_{j0}	F_{j1}	Φ	$A_\parallel$
n_0/v_{Tj}^3	$(n_0/v_{Tj}^3)\rho_s/L_\perp$	$(T_{e0}/e)\rho_s/L_\perp$	$(qR\rho_s B_{\mathrm{ref}}\beta_e/L_\perp)\rho_s/L_\perp$

of B with respect to B_{ref}. We use as velocity space coordinates the parallel velocity $v_\parallel$ and the magnetic moment μ. The dependent variables, on the other hand, are normalized according to Table II. Here, the distribution function F_j is broken up into an equilibrium part F_{j0} and a perturbed part F_{j1}. In these units, the gyrokinetic Vlasov equation reads

$$\frac{\partial g_j}{\partial t}+\left[\omega_n+\omega_{Tj}\left(v_\parallel^2+\mu\hat{B}-\tfrac{3}{2}\right)\right]F_{j0}\frac{\partial \chi_j}{\partial y}+\left(\frac{\partial \chi_j}{\partial x}\frac{\partial G_j}{\partial y}-\frac{\partial \chi_j}{\partial y}\frac{\partial G_j}{\partial x}\right)+\frac{\mu\hat{B}+2v_\parallel^2}{2\sigma_j\hat{B}}\left(\mathcal{K}_x\frac{\partial G_j}{\partial x}+\mathcal{K}_y\frac{\partial G_j}{\partial y}\right)+\alpha_j v_\parallel\frac{\partial G_j}{\partial z}-\frac{\alpha_j}{2}\mu\hat{B}^2\epsilon_t\sin z\frac{\partial F_{j1}}{\partial v_\parallel}=0, \tag{1}$$

with the curvature terms

$$\mathcal{K}_x=-2\frac{L_\perp}{R_0}\sin z,\quad \mathcal{K}_y=-2\frac{L_\perp}{R_0}(\cos z+\hat{s}z\sin z)$$

and the definitions (where an overbar indicates a gyroaveraged quantity)

$$g_j=F_{j1}+\sigma_j\alpha_j v_\parallel F_{j0}\hat{\epsilon}\beta_e\bar{A}_{1\parallel},\quad G_j=g_j+\sigma_j\chi_j F_{j0},$$

$$\chi_j=\bar{\Phi}_1-\alpha_j v_\parallel\hat{\epsilon}\beta_e\bar{A}_{1\parallel},$$

as well as

$$\sigma_j=\frac{e_j}{e}\frac{T_{e0}}{T_{j0}},\quad \alpha_j=\frac{v_{Tj}}{c_s}\frac{L_\perp}{qR},\quad \hat{\epsilon}=\left(\frac{qR}{L_\perp}\right)^2,$$

$$\beta_e=\frac{4\pi n_0 T_{e0}}{B_{\mathrm{ref}}^2},$$

$$\omega_n=\frac{L_\perp}{L_n}=-\frac{L_\perp}{n_0}\frac{dn_0}{dx},\quad \omega_{T_j}=\frac{L_\perp}{L_{T_j}}=-\frac{L_\perp}{T_{j0}}\frac{dT_{j0}}{dx}.$$

As an equilibrium distribution we take a Maxwellian which reads

$$F_{j0}(v_\parallel,\mu)=\pi^{-3/2}e^{-(v_\parallel^2+\mu\hat{B})}$$

in normalized units. Moreover, we employ the well-known $\hat{s}-\alpha$ geometry[17] (with α set to zero) in this paper.

The gyrokinetic Maxwell equations used to determine the self-consistent electromagnetic fields are the gyrokinetic Poisson equation

$$\sum_j e_j\sigma_j[1-\Gamma_0(b_j)]\Phi_1=\sum_j e_j\pi\hat{B}\int J_0(\lambda_j)g_j dv_\parallel d\mu \tag{2}$$

and the gyrokinetic Ampère's law

$$\left(\nabla_\perp^2-\frac{1}{2}\hat{\epsilon}\beta_e\sum_j\sigma_j\alpha_j^2\frac{e_j}{e}\Gamma_0(b_j)\right)A_{1\parallel}=-\sum_j\alpha_j\frac{e_j}{e}\pi\hat{B}\int v_\parallel J_0(\lambda_j)g_j dv_\parallel d\mu. \tag{3}$$

Here, the Bessel function J_0 and the function $\Gamma_0(b_j)=e^{-b_j}I_0(b_j)$ (where I_0 is the modified Bessel function) have been introduced. The arguments λ_j and b_j are defined, respectively, as

$$\lambda_j^2=2\mu\hat{B}b_j,\quad b_j=-\frac{m_j}{m_i}\frac{T_{j0}}{T_{e0}}\frac{e^2}{e_j^2}\frac{\nabla_\perp^2}{\hat{B}^2}.$$

These equations are solved by the GENE code which has been modified and upgraded with respect to the version described in Ref. 18. It uses a flux tube[19] as simulation domain, with periodic boundary conditions in the perpendicular plane. The new GENE code uses (compact) finite differences of at least fourth order in phase space, and an explicit Runge–Kutta time stepping scheme of third order. The code has been benchmarked successfully against semianalytical results and numerical results obtained with the GS2 code[20] as is shown in Refs. 21 and 22. For further details concerning the code, see Ref. 22.

For completeness, we also give the definitions for the transport fluxes. Although the nominal value of β_e is nonzero, it is so small that the electromagnetic contributions to the transport coefficients may be safely neglected. The electrostatic transport of particles and heat across magnetic flux surfaces is given, respectively, by

$$\Gamma=\left\langle\int F_{j1}v'_{E,x}d^3v\right\rangle$$

and

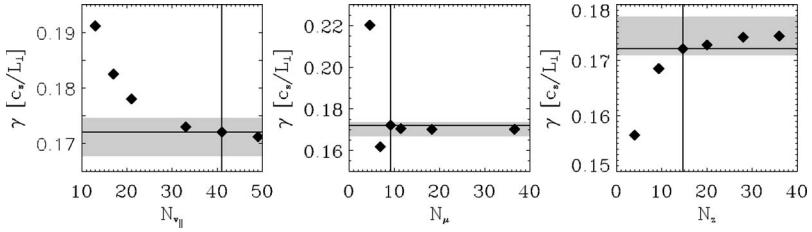

FIG. 1. Convergence tests: Linear growth rate of trapped electron mode as a function of velocity space resolution and the number of parallel grid points. Here, we used the nominal physical parameters and $k_y\rho_s=0.3$. The lines indicate the base case, and the shaded region marks a deviation of less than ±2% with respect to the point with the highest resolution.

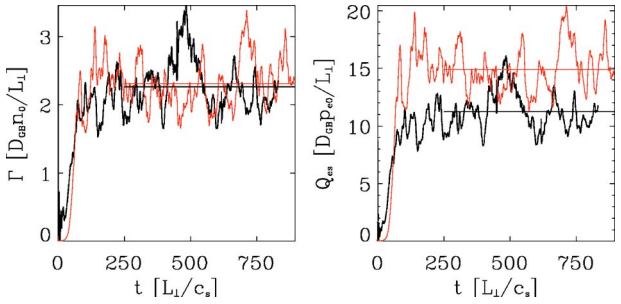

FIG. 2. (Color online). Time traces of TEM-induced particle flux Γ and electrostatic electron heat flux Q_{es} for the nominal parameters and an ion-to-electron mass ratio of 1836 (black) and 400 (gray).

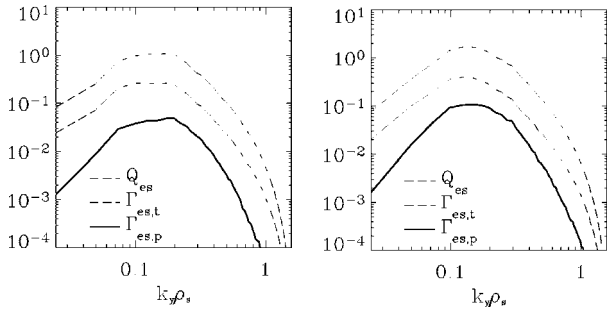

FIG. 3. Transport spectra of TEM turbulence for hydrogen mass ratio (left) and reduced mass ratio (right). Shown are the electrostatic heat flux Q_{es}, the trapped electron flux $\Gamma_{es,t}$, and the passing electron flux $\Gamma_{es,p}$. Thick lines indicate negative values.

$$Q_j = \left\langle \int (v_\parallel^2 + \mu \hat{B}) F_{j1} v'_{E,x} d^3 v \right\rangle$$

in normalized units. Here, $v'_E = -(c/B^2) J_0(\lambda_j) \Phi \times \mathbf{B}$ is the modified $\mathbf{E} \times \mathbf{B}$ drift velocity, and the angular brackets denote spatial averaging over the entire simulation domain.

B. Physical and numerical parameters

As mentioned above, there have been many tokamak experiments in recent years which are characterized by dominant electron heating and rather cold ions.[10–13] Inspired by these studies, we choose the following baseline set of physical parameters: $R/L_n = 3$, $R/L_{T_e} = 6$, $R/L_{T_i} = 0$, $\epsilon_t \equiv r/R = 0.16$, $q = 1.4$, $\hat{s} = 0.8$, $T_e/T_i = 3$, $\beta_e \equiv 4\pi n_e T_{e0}/B_{\mathrm{ref}}^2 = 0.001$. Moreover, we choose $R/L_\perp = 3$ and always hold this number fixed while the normalized gradients (such as R/L_n) are varied in parameter scans. (Note that $L_\perp$ is used for normalization, not L_n, etc.)

Nearly all of our simulations are done with boxes of $L_x \times L_y = 152.8\rho_s \times 256\rho_s$ in the perpendicular directions, and one connection length, $2\pi qR$, in the parallel direction. This three-dimensional spatial simulation domain is represented by $128 \times 128 \times 16$ grid points. The velocity space variables $v_\parallel$ and μ run from $-v_{\mathrm{cut}}$ to v_{cut} ($v_{\mathrm{cut}} = 3v_{Tj}$) and from zero to $9T_{j0}/B_{\mathrm{ref}}$, respectively. Here, 40×8 grid points are typically used. In Ref. 21, we showed that a reduced version of the code is able to reproduce the frequencies and damping rates of kinetic shear Alfvén waves with high precision. In this context, it has been found that about 30 parallel velocity grid points are necessary to obtain convergence. These tests have been repeated for trapped-electron modes, leading to similar results. In Fig. 1, the respective linear growth rates are shown as a function of the numerical parameters $N_{v_\parallel}$, N_μ, and N_z for the nominal physical parameters mentioned above and $k_y\rho_s = 0.3$. Here, the numerical parameters have been varied about the standard values of $N_{v_\parallel} = 41$, $N_\mu = 8$, and $N_z = 16$. The perpendicular grid consisted of 16×16 points, and the box size was $4.17\rho_s \times 20.94\rho_s$. As can be inferred from Fig. 1, the velocity space resolution used in our simulations is (more than) sufficient to represent collisionless trapped-electron modes.

From a computational point of view, a key challenge of the present simulations is the time scale separation between the perpendicular turbulent motion and the fast parallel electron dynamics. Roughly speaking, the numerical cost increases in proportion to the square root of the ion-to-electron mass ratio. To allow for a larger number of runs, we therefore attempted to lower the mass ratio from $m_i/m_e = 1836$ (hydrogen) to $m_i/m_e = 400$. The time traces of particle and electron heat fluxes for two runs using the above nominal parameters and these different mass ratios are shown in Fig. 2. While the saturation levels of the particle flux are basically identical, the electron heat transport increases from ~ 11 for the hydrogen mass ratio to ~ 15 for the reduced one. The respective transport spectra are shown in Fig. 3. Obviously, there is no significant qualitative difference between both simulations, and the quantitative differences are reasonably small. These findings motivated us to use the reduced mass ratio for all further computations—a procedure which saves half of the computer time. Physically, this is in line with the notion that TEMs tend to be dominated by trapped electrons, not passing ones—and that the former are less susceptible to changes in the mass ratio than the latter.

III. BASIC TURBULENCE CHARACTERISTICS

A. Spatial mode structure

First, we would like to investigate the spatial structure of TEM turbulence. A typical snapshot of contours of different plasma quantities is shown in Fig. 4. One observes elongated vortices (streamers) with a radial extent of up to $60\rho_s$. Such structures have also been observed in nonlinear simulations of electron temperature gradient (ETG) modes[18] and resistive ballooning (RB) modes.[23] However, the TEM streamers seem to be somewhat less pronounced than their ETG and

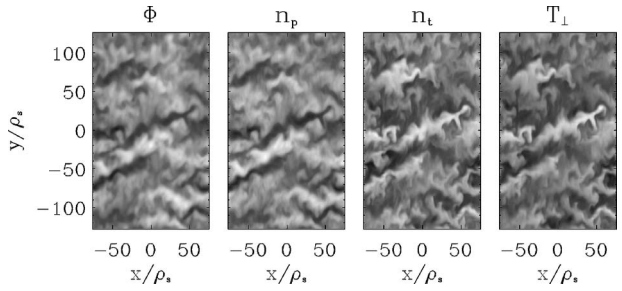

FIG. 4. Typical snapshot of contour plots of the electrostatic potential, the passing/trapped electron density, and the perpendicular electron temperature.

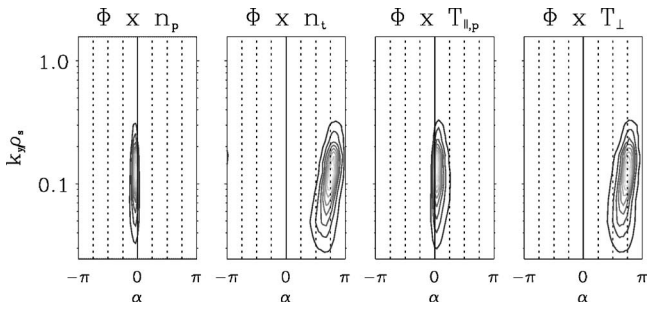

FIG. 5. Phase relations between the electrostatic potential and the passing/trapped electron density as well as the parallel/perpendicular electron temperature.

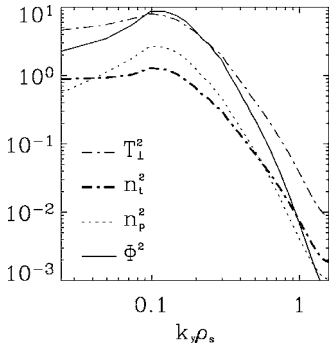

FIG. 6. Squared amplitude spectra in k_y space for several fluctuating plasma quantities.

RB counterparts. A careful inspection of the four quantities displayed in Fig. 4 reveals strong correlations between fluctuations of the electrostatic potential and the passing electron density as well as between fluctuations of the trapped-electron density and the perpendicular electron temperature. These similarities are not incidental. The first of these correlations has its origin in the nearly adiabatic response of passing electrons. Since the latter can move freely along the magnetic field lines, they adjust to changes in the electrostatic potential almost immediately. The origin of the second similarity becomes clear if we recall that the trapped electrons have a small parallel velocity and a large perpendicular one. As the perpendicular velocity accounts for the perpendicular temperature, the trapped electrons carry the main part of $T_\perp$. This leads to the strong correlation between the density of the trapped electrons and the perpendicular electron temperature.

B. Cross phases

Further insight into the structure of the turbulence may be gained by investigating the cross phase relations between the electrostatic potential and the three remaining quantities shown in Fig. 4. To obtain the plots shown in Fig. 5, the following steps have to be taken. First, one Fourier transforms the respective pair of fluctuating quantities in the periodic y direction for each value of x (radial coordinate), z (parallel coordinate), and time t. Then, the cross phases α are determined as a function of k_y for each point in (x,z,t) space. Finally, a weighted probability distribution function (PDF) in (α,k_y) space is determined and the contours of such PDFs are plotted. The weighting factor is given by the product of the absolute values of the k_y components of the two quantities under consideration. (This weighting procedure helps to make the respective contour plots a little cleaner, especially in the high k_y region.) In Fig. 5, light colors denote regions of high correlation. Interestingly, fluctuations centered around $k_y\rho_s \sim 0.1-0.2$, i.e., in the transport region (according to Fig. 3), exhibit clearly defined cross phases, whereas at higher k_y, the latter are randomly distributed between $-\pi$ and π.

The phase angle between Φ and n_p is close to zero. This is again a signature of the passing electrons' near adiabaticity. A similar phase relation is observed for the parallel temperature. The remaining two plots both show a distinct phase angle of about $3\pi/4$. To understand the similarity of the first and third graphs as well as the second and fourth graphs in Fig. 5, one must again recall that passing electrons have a relatively large parallel velocity, whereas trapped electrons have a relatively large perpendicular velocity. So the parallel temperature is carried mainly by passing electrons, and the perpendicular temperature by the trapped ones.

C. Transport and amplitude spectra

Since a cross phase close to zero (or π) is indicative of a small flux, we expect that the particle transport is mainly carried by the trapped electrons and that the electron heat flux is dominated by the perpendicular temperature. Furthermore we anticipate that the transport is driven primarily in the range $k_y\rho_s \sim 0.1-0.2$, since only in this part of the wave number spectrum a distinct phase relation exists. In Fig. 3 the k_y spectra of the transport fluxes are shown. Here, thick lines indicate negative values, so that the passing electrons are actually transported inwards (up-gradient), in contrast to the trapped electrons which are transported outwards (down-gradient) and which dominate the particle transport. It should be emphasized that the maximum of the transport takes place at about $k_y\rho_s \sim 0.12$, which is way below the position of the fastest growing linear TEM ($k_y\rho_s \sim 0.4$). Typical amplitude spectra are shown in Fig. 6. One can clearly identify an energy input region around $k_y\rho_s \sim 0.12$, an inertial range characterized by the power law $|\Phi|^2 \propto k_y^{-5.1}$, and a dissipation range at high k_y.

D. Parallel mode structure

Next, we would like to characterize the mode structure along the field lines. To this end, the squared amplitudes are averaged over perpendicular planes (and time). Some examples are shown in Fig. 7. The electrostatic potential, the trapped-electron density, and the perpendicular electron temperature are all peaked in the outboard midplane (i.e., at $z=0$) whereas the passing electron density is nearly constant along field lines. This is due to the following reasons. Trapped particles have their largest density at $z=0$, since this is the only point that *all* of them pass in the course of their bounce motion, irrespective of their turning points. As mentioned before, the trapped particles are mainly responsible for the perpendicular temperature, so $T_\perp$ also peaks at $z=0$.

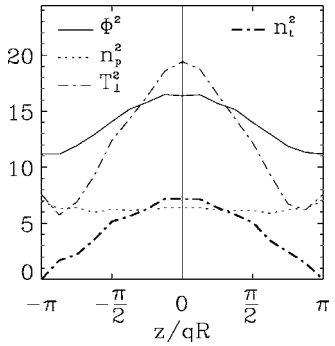

FIG. 7. Parallel mode structure: Squared amplitude profiles in z space for several fluctuating plasma parameters.

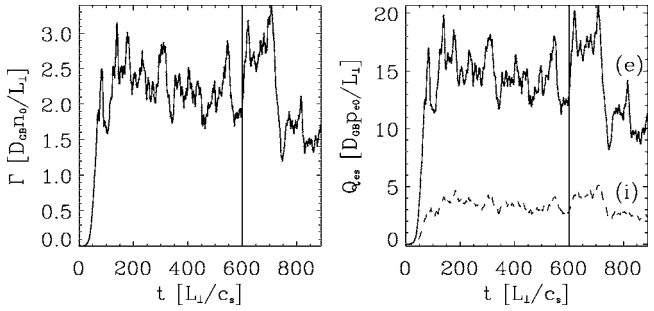

FIG. 9. Time traces of the particle and electron/ion heat fluxes for nominal parameters. For $t \geqslant 600$, zonal flows are artificially suppressed.

Passing electrons, on the other hand, are influenced only moderately by variations of the magnetic field strength. This is reflected in a passing electron density which is more or less constant in the z direction. In Fig. 8, the parallel structure of the transport fluxes is shown. Both the particle and the electron heat transport exhibit the same ballooning structure as various quantities in Fig. 7, i.e., the transport is not evenly distributed over the entire domain but centered around the outboard midplane. The only exception is the particle flux carried by passing electrons, but this contribution is subdominant for the present set of physical parameters.

E. The role of zonal flows

It is well known that in the case of ITG turbulence, zonal flows of considerable strength can be generated by the turbulence itself and may in turn shear apart the existing turbulent vortices. Zonal flow spin-up may thus lead to a substantial reduction of the induced turbulent transport.[24,25] In order to assess the degree to which TEM turbulence is affected by zonal flow dynamics, we zeroed them out in the course of a run and monitored the effect of this change on the transport levels. In Fig. 9, the time traces of the particle and electron/ion heat fluxes are presented for such a nonlinear simulation. Beginning at $t=600$, the zonal component of the electrostatic potential is artificially suppressed. In analogy to the ITG case, one might expect that the transport levels increase strongly. However, although this pure TEM system clearly is affected by the sudden absence of zonal flows, one does not observe a drastic change in the fluxes.

The time-averaged k_x spectrum of the zonal component of the electrostatic potential is shown in Fig. 10. For $k_x\rho_s \gtrsim 0.4$, this spectrum exhibits a power law behavior. In this region of k_x space, the squared zonal potential is characterized by an exponent of about -5.7. This number is rather close to the exponent in the inertial range of the k_y spectrum, where we measured a value of about -5.1. The shearing rate corresponding to these zonal potential fluctuations is readily calculated as $\omega_E = dv_{Ey}/dx = d^2\Phi/dx^2$. The sum over all scales yields a total shearing rate of about $\omega_E \approx 0.2$ which is of the order of the maximum linear growth rate of the TEMs. Therefore, the zonal flow content is by no means negligible. However, for the zonal flows to be the dominant nonlinear saturation mechanism, the shearing rate would have to be much larger than the maximum linear growth rate,[26] and this is clearly not the case here. So the influence of zonal flow dynamics on the transport level of TEM turbulence is small. Further studies will have to investigate how general this finding is and if there are other regions in parameter space in which zonal flows are indeed dominant. Also, it will be interesting to find out what the precise nonlinear saturation mechanism is, given the relative weakness of $\mathbf{E}\times\mathbf{B}$ shearing. While such mechanisms may be found in the literature (see, e.g., Ref. 18), it is presently unclear which one (if any) of them applies to the present situation. We leave this question for future work.

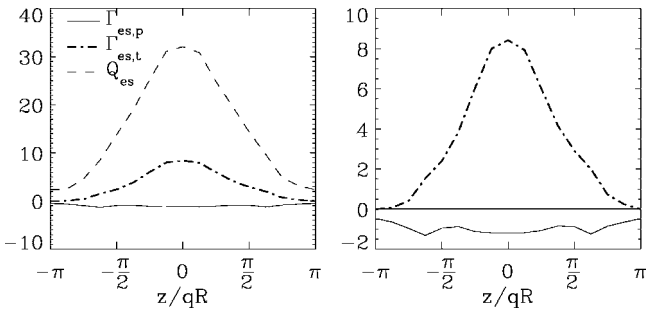

FIG. 8. Parallel profiles of the heat and particle fluxes carried by the electrons. The particle fluxes are shown again on the right-hand side in a zoomed-in fashion.

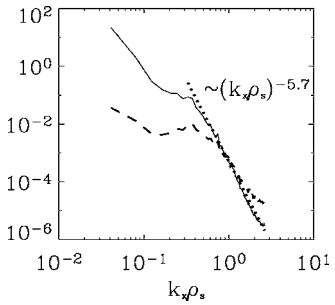

FIG. 10. Spectra of the zonal component of Φ (solid) and of the $\mathbf{E}\times\mathbf{B}$ shearing rate (dashed) in k_x space.

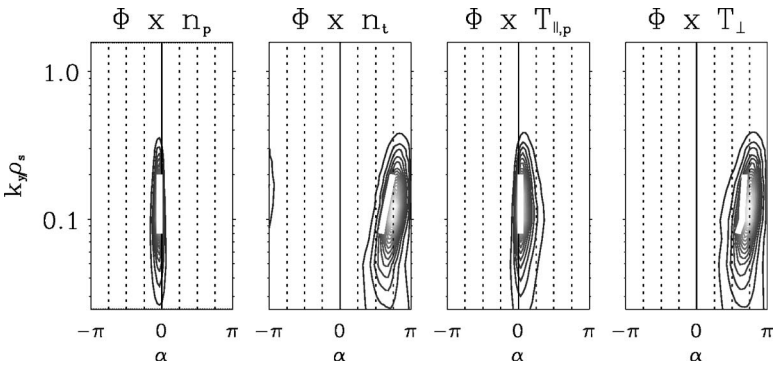

FIG. 11. Comparison of linear (thick white lines) and nonlinear (contour lines) cross phases.

F. Persistence of the linear mode structure

Finally, we would like to address the question to which degree the nonlinear mode structure in the saturated turbulent state resembles that of the underlying linear microinstabilities. One way to approach this issue is by comparing the cross phases of exponentially growing linear modes and quasistationary nonlinear modes. Such a comparison is presented in Fig. 11. This figure contains the same information as Fig. 5, but now the linear cross phases are also shown. One can see that the linear cross phases are quite close to the nonlinear ones in the transport-dominating range of scales. This may be taken as a clear signature of the persistence of the linear mode structure in the nonlinear regime. At short wavelengths, the fluctuations are randomized, whereas at long wavelengths, the TEM system partially respects the underlying linear drive mechanism.

Based on this finding, we were able to construct the following (quasi)linear transport model which will be used in the remainder of this paper for comparison with the nonlinear simulations. Assuming $k_x=0$ and $\alpha=0$, we have

$$\langle k_\perp^2 \rangle = k_y^2(1+\hat{s}^2\langle\theta^2\rangle) \tag{4}$$

for the average value of $k_\perp^2$ where θ is an extended, anglelike coordinate in the field-line direction and

$$\langle\theta^2\rangle \equiv \frac{\int \theta^2 |\phi_{k_y}(\theta)|^2 d\theta}{\int |\phi_{k_y}(\theta)|^2 d\theta}. \tag{5}$$

Here, the weighting is done in terms of the (complex-valued) eigenfunction $\phi_{k_y}(\theta)$ for a given set of plasma parameters and a given value of k_y. Consequently, holding all plasma parameters fixed, $\gamma/\langle k_\perp^2\rangle$ is a function of k_y (see Fig. 12). Based on these results, one can estimate the electron heat flux Q_e via

$$\frac{Q_e}{n_{e0}T_{e0}/R} = \mathcal{C}\max_{k_y}\left[\frac{\gamma}{\langle k_\perp^2\rangle}\right]\frac{R}{L_{T_e}}, \tag{6}$$

and the ion heat flux Q_i as well as the particle flux Γ via the ratios of the corresponding quasilinear estimates. The additional factor of R/L_{T_e} mediates between χ_e and Q_e, and the free parameter $\mathcal{C}$ is determined such that Q_e agrees with the nonlinear simulation result for the base case parameters. Details may be found in a separate publication.

IV. SOME PARAMETER DEPENDENCES

A. Safety factor *q*

As has been known for quite some time, empirical models for the electron heat flux generally reproduce experimental data reasonably well only if the electron heat diffusivity χ_e scales with the safety factor q like $\chi_e \approx q^\tau$, where $1 \lesssim \tau \lesssim 2$.[13] In many cases, the experimentally observed value of χ_e is attributed largely to TEM turbulence. However, the scaling of TEM-induced transport with q is unknown, and thus the q dependence employed in empirical models has no firm theoretical support. We therefore performed a q scan around the base case parameters to close this gap. The results of a three-point scan are shown in Fig. 13. Indeed, one observes a rather strong increase of χ_e with increasing safety factor. To quantify this result, one may try to express the simulation data in terms of a power law. One thus obtains $\tau \approx 1.7$ which lies somewhere in the middle of the interval mentioned above. Although this particular number is unlikely to be universal, it is very encouraging and seems to justify *a posteriori* the use of transport expressions with $1 \lesssim \tau \lesssim 2$ for TEM-driven turbulence.

For comparison, the results of our simple transport model are shown in Fig. 13 as dashed lines. Interestingly, the strong q dependence is fairly well reproduced. (Note that the model contains a universal prefactor which has been set to match the electron heat flux in the standard case.) This finding is in stark contrast to the very weak q scalings found in

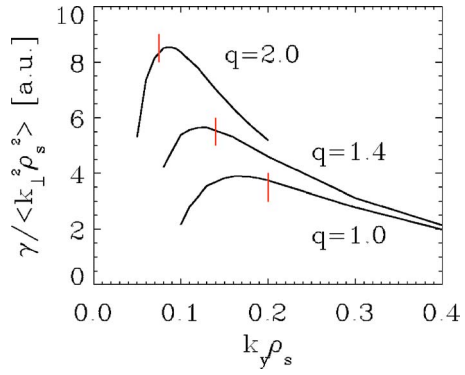

FIG. 12. (Color online). The black lines show the transport spectra as estimated by our simple transport model for different q values; the vertical lines indicate the position of the peak of the respective *turbulent* transport spectrum.

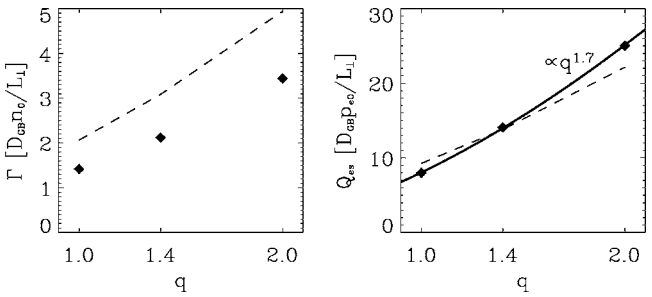

FIG. 13. Particle and electron heat fluxes as a function of the safety factor q. The predictions of a simple (quasi)linear transport model are shown for comparison (dashed lines).

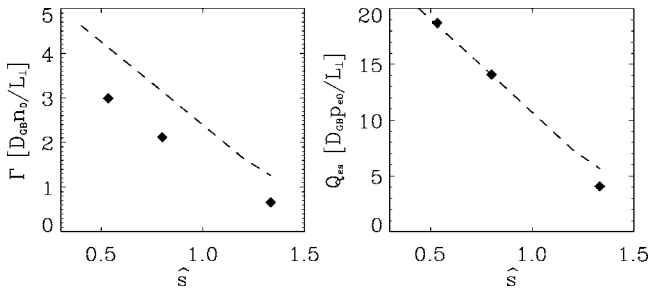

FIG. 15. Electrostatic electron transport fluxes of TEM turbulence as a function of magnetic shear.

the framework of conventional (quasi)linear models (see, e.g., Ref. 27). Therefore, two questions arise: (1) What is the origin of the observed q scaling? (2) Why is our (quasi)linear transport model able to capture the changes observed in the nonlinear simulations while others cannot? The answers to both questions have to do with the fact that the peak of k_y spectrum of turbulent transport is approximately inversely proportional to q (see Fig. 12), like in ETG turbulence.[28] This means that the turbulent eddies increase in size with increasing safety factor. In a random walk picture of turbulent transport, this translates directly into the transport boost mentioned above. Our simple transport model retains this shift in spatial scales. It contains a rule by which the appropriate value of k_y is determined for each given set of plasma parameters. On the other hand, most conventional transport models work at constant (and larger) values of k_y, and therefore miss the strong q dependence. The physical reason for the q dependence both for ETG and for TEM-driven transport is that the transport-dominating scales in the turbulent system tend to follow the low-k_y cutoff of the linear mode spectrum which is determined by a balance of drive (which is proportional to v_{Ex} or k_y and vanishes for $k_y=0$) and Landau damping (which scales like the inverse connection length or $1/q$).

B. Other plasma parameters

Next, we will study the dependence of TEM-induced transport on the inverse aspect ratio $\epsilon_t \equiv r/R$, and on magnetic shear $\hat{s} \equiv (r/q)dq/dr$. The corresponding simulation results are shown in Figs. 14 and 15. A change of the inverse aspect ratio is reflected in a change of the fraction of trapped particles. The latter scales as $\epsilon_t^{1/2}$, and therefore the linear growth rates of TEMs increase with ϵ_t. This linear drive enhancement carries over into the nonlinear regime. Similarly, the drive reduction caused by large magnetic shear leads to a decrease of the transport level, see Fig. 15.

The dependence of the turbulent transport on the normalized density gradient is somewhat more complicated as can be seen in Fig. 16. The particle flux exhibits a continuous (and more or less linear) increase with R/L_n, as one might have expected. The same is true for the ion heat flux which is solely density gradient driven in the absence of a finite ion temperature gradient. In contrast to that, the electron heat flux saturates for $R/L_n \gtrsim 3$, i.e., it becomes almost independent of the density gradient. In this "steep-gradient" regime, the particle and electron heat fluxes decouple, and our simple transport model fails. Although we expect the cause to be a nonlinear effect, zonal flows can be excluded for two reasons. First, they would affect all transport channels in the same way, and second, we confirmed that they stay subdominant even in the high-R/L_n regime by zeroing them out. Further investigations along these lines are left for the future.

V. SUMMARY AND CONCLUSIONS

In summary, we investigated some basic properties of collisionless TEM turbulence in tokamaks by means of massively parallel gyrokinetic Vlasov simulations. For our nominal parameters, the spatial mode structure exhibits streamer-like structures and relatively weak zonal flows. Cross phase diagnostics suggest an interpretation of the dynamics on the transport-dominating scales in terms of remnants of linear modes embedded in a sea of smaller-scale eddies. We also investigated the dependence of the transport level on several

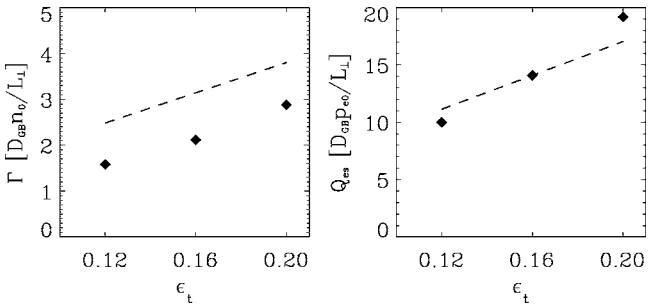

FIG. 14. Electrostatic electron transport fluxes of TEM turbulence as a function of the inverse aspect ratio.

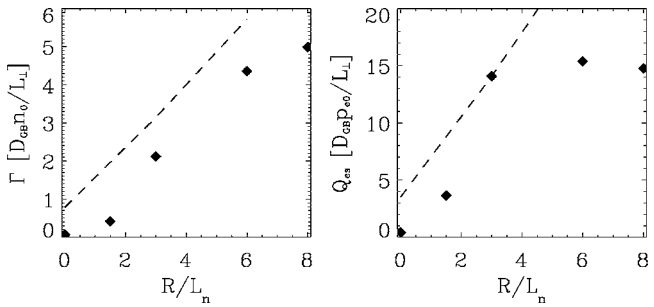

FIG. 16. Electrostatic transport fluxes of TEM turbulence as a function of the normalized density gradient.

plasma parameters and compared our nonlinear simulation results with those of a simple (quasi)linear transport model. Both approaches yield a superlinear scaling of the electron heat diffusivity with the safety factor q, as is suggested by analyses of experimental data. This finding can be explained by a downshift of the peak of the nonlinear transport spectrum in k_y space with increasing q. This peak is observed to follow the low-k_y cutoff of TEMs which reflects a balance of Landau damping ($\propto 1/q$) and linear drive ($\propto k_y$). The dependence of the transport levels on the inverse aspect ratio and on magnetic shear is captured well by our simple (quasi)linear transport model. Only in the high-density-gradient regime, we found a (currently unexplained) discrepancy between the model and the nonlinear runs.

These studies of collisionless TEM turbulence seem to allow for at least two general conclusions. First, one learns that there are experimentally relevant parameter regimes in which turbulent transport in magnetized fusion plasmas can be described in terms of linear remnants embedded in a sea of turbulence. Interestingly, this basic character is shared by many other complex systems in both physics and engineering (see, e.g., Ref. 29). Second, one learns that one has to be very careful in assessing simple (quasi)linear models of turbulent transport in magnetoplasmas. It is very tempting to either overestimate or underestimate their capabilities. Surely, turbulent fusion plasmas are full of (nonlinear) surprises which call for *ab initio* simulations, but on the other hand, one should not dismiss these models too readily. In particular, it seems possible to further improve (quasi)linear transport models beyond their status quo.

[1] P. C. Liewer, Nucl. Fusion **25**, 543 (1985).
[2] H. Nordman, J. Weiland, and A. Jarmén, Nucl. Fusion **30**, 983 (1990).
[3] S. E. Parker, W. W. Lee, and R. A. Santoro, Phys. Rev. Lett. **71**, 2042 (1993).
[4] A. M. Dimits, T. J. Williams, J. A. Byers, and B. I. Cohen, Phys. Rev. Lett. **77**, 71 (1996).
[5] R. D. Sydora, V. K. Decyk, and J. M. Dawson, Plasma Phys. Controlled Fusion **38**, A281 (1996).
[6] M. A. Beer and G. W. Hammett, Phys. Plasmas **3**, 4018 (1996).
[7] D. Ross and W. Dorland, Phys. Plasmas **9**, 5031 (2002).
[8] J. Candy and R. E. Waltz, J. Comp. Physiol. **186**, 545 (2002).
[9] S. E. Parker, Y. Chen, and W. Wan, Phys. Plasmas **11**, 2594 (2004).
[10] F. Ryter, G. Tardini, F. D. Luca, H.-U. Fahrbach, F. Imbeaux, A. Jacchia, K. K. Kirov, F. Leuterer, P. Mantica, A. G. Peeters *et al.*, Nucl. Fusion **43**, 1396 (2003).
[11] F. Ryter, F. Leuterer, G. Pereverzev, H.-U. Fahrbach, J. Stober, W. Suttrop, and ASDEX Upgrade Team, Phys. Rev. Lett. **86**, 2325 (2001).
[12] C. Angioni, A. G. Peeters, F. Ryter, F. Jenko, G. D. Conway, T. Dannert, H.-U. Fahrbach, M. Reich, W. Suttrop, ASDEX Upgrade Team, and L. Fattorini, Phys. Plasmas **12**, 040701 (2005).
[13] X. Garbet, P. Mantica, F. Ryter, G. Cordey, F. Imbeaux, C. Sozzi, A. Manini, E. Asp, V. Parail, R. Wolf *et al.*, Plasma Phys. Controlled Fusion **46**, 1351 (2004).
[14] T. S. Hahm, Phys. Fluids **31**, 2670 (1988).
[15] T. Hahm, W. Lee, and A. Brizard, Phys. Fluids **31**, 1940 (1988).
[16] A. Brizard, Phys. Fluids B **1**, 1381 (1989).
[17] J. W. Connor, R. J. Hastie, and J. B. Taylor, Phys. Rev. Lett. **40**, 396 (1978).
[18] F. Jenko, W. Dorland, M. Kotschenreuther, and B. N. Rogers, Phys. Plasmas **7**, 1904 (2000).
[19] M. A. Beer, S. C. Cowley, and G. W. Hammett, Phys. Plasmas **2**, 2687 (1995).
[20] M. Kotschenreuther, G. Rewoldt, and W. Tang, Comput. Phys. Commun. **88**, 128 (1995).
[21] T. Dannert and F. Jenko, Comput. Phys. Commun. **163**, 67 (2004).
[22] T. Dannert, Ph.D. thesis, Technische Universität München, 2005; see http://tumb1.biblio.tu-muenchen.de/publ/diss/ph/2005/dannert.pdf
[23] P. Beyer, S. Benkadda, X. Garbet, and P. Diamond, Phys. Rev. Lett. **85**, 4892 (2000).
[24] A. Hasegawa and M. Wakatani, Phys. Rev. Lett. **59**, 1581 (1987).
[25] G. W. Hammett, M. A. Beer, W. Dorland, S. C. Cowley, and S. A. Smith, Plasma Phys. Controlled Fusion **35**, 973 (1993).
[26] T. S. Hahm, M. A. Beer, Z. Lin, G. W. Hammett, W. W. Lee, and W. M. Tang, Phys. Plasmas **6**, 922 (1999).
[27] A. Peeters, C. Angioni, M. Apostoliceanu, F. Jenko, F. Ryter, and ASDEX Upgrade Team, Phys. Plasmas **12**, 022505 (2005).
[28] F. Jenko, W. Dorland, A. Kendl, and D. Strintzi, *Theory of Fusion Plasmas* (Società Italiana di Fisica, Bologna, 2002), p. 157.
[29] C. Daw and J. Halow, Chaos **14**, 370 (2004).